Computers and Mathematics with Applications (2020)

Contents lists available at ScienceDirect

Computers and Mathematics with Applications

journal homepage: www.elsevier.com/locate/camwa

A Finite-Volume Scheme for Gradient Flow Equations with Non-Homogeneous Diffusion

Julien Mendes[a,*], Antonio Russo[b,*], Sergio P. Perez[b,c,*], Serafim Kalliadasis[b,**]

[a]*Institut de Mathématiques de Toulouse, INSA de Toulouse, Toulouse, France*
[b]*Department of Chemical Engineering, Imperial College London, London, United Kingdom*
[c]*Department of Mathematics, Imperial College London, London, United Kingdom*

ARTICLE INFO

Article history:
Received 2019
Received in final form 20XX
Accepted 20XX
Available online 20XX

Communicated by Editor name

Non-homogeneous baths, finite-volume schemes, dynamical-density functional theory

ABSTRACT

We develop a first- and second-order finite-volume scheme to solve gradient flow equations with non-homogeneous properties, obtained in the framework of dynamical-density functional theory. The scheme takes advantage of an upwind approach for the space discretization to ensure positivity of the density under a CFL condition and decay of the discrete free energy. Our computational approach is used to study several one- and two-dimensional systems, with a general free-energy functional accounting for external fields and inter-particle potentials, and placed in non-homogeneous thermal baths characterized by anisotropic, space-dependent and time-dependent properties.

1. Introduction

A wide spectrum of applications in biology [1, 2, 3, 4], chemistry [5, 6, 7] and engineering [8, 9] require a deep understanding of the dynamical evolution of colloidal fluids in thermal baths. The large number of degrees of freedom and complex interactions between the constituent components of these systems makes them prohibitive to analytical work and, consequently, we have to resort to computational approaches. Atomistic simulations, such as molecular dynamics or simulations of macroscopic deterministic-stochastic continuum models, such as Navier-Stokes– Landau-Lifshitz fluctuating-hydrodynamics [10, 11, 12, 13] are often used to describe simple and complex fluids.

Atomistic simulations can provide an accurate description of the microscopic properties and reveal finer details on the microscale [14]. But their high computational cost limits their applicability. At the same time, despite drastic improvements in computational power, atomistic simulations are still only applicable for small fluid volumes. On the other side, macroscopic continuum simulations are much less computationally expensive, but microscopic information is averaged out and lost.

*These authors are co-first and contributed equally to this work.
**Corresponding author.
e-mail: s.kalliadasis@imperial.ac.uk (Serafim Kalliadasis)

A compromise between atomistic simulations and macroscopic continuum models can be achieved by density-functional theory (DFT) [15, 16]. DFT is able to retain the microscopic details of a macroscopic system at a computational cost significantly lower than that used in atomistic simulations. Its cornerstone is a density-dependent Helmholtz free-energy functional, known as grand potential, which is minimum at equilibrium. This functional encapsulates all interactions in the system and external fields. Dynamic DFT (DDFT) is an extension of DFT away from equilibrium and in its simplest version it states that the dynamic variation of a conserved-order parameter (often the density) is given by the gradient of a flux with an advective part proportional to the local flow field and a diffusive part proportional to the gradient of the Helmholtz free-energy functional [17, 18, 19]. (D)DFT has been used successfully to study the wetting behaviour of fluids in contact with solid surfaces, including wetting phase transitions and associated critical phenomena [8, 9, 20, 21, 22, 23, 24, 25] and complex dynamical fluid behaviour [18, 19, 26, 27].

In the presence of inertia, DDFT consists of the following system of equations for the time-evolution of density ρ and velocity $\mathbf{v}$ fields [13, 18, 19, 28]:

$$\begin{aligned} &\partial_t \rho(\mathbf{r},t) + \boldsymbol{\nabla}_{\mathbf{r}} \cdot \left(m^{-1} \rho(\mathbf{r},t) \mathbf{v}(\mathbf{r},t) \right) = 0, \\ &\partial_t \left(\rho(\mathbf{r},t) \mathbf{v}(\mathbf{r},t) \right) + \boldsymbol{\nabla}_{\mathbf{r}} \cdot \left(\rho(\mathbf{r},t) \mathbf{v}(\mathbf{r},t) \otimes \mathbf{v}(\mathbf{r},t) \right) + \rho(\mathbf{r},t) \boldsymbol{\nabla}_{\mathbf{r}} \frac{\delta \mathcal{E}[\rho]}{\delta \rho(\mathbf{r},t)} + \boldsymbol{\Gamma} \rho(\mathbf{r},t) \mathbf{v}(\mathbf{r},t) = 0, \end{aligned} \tag{1}$$

where m is the mass of the colloidal particles, $\mathcal{E}[\rho]$ is the free energy functional and $\boldsymbol{\Gamma}$ is the friction tensor that depends on the interactions between the colloidal and bath particles. In the strong damping limit, $m^{-1}\boldsymbol{\Gamma} \to \infty$, i.e. when the relaxation time of the density is much larger than the momentum, the terms $\boldsymbol{\nabla}_{\mathbf{r}} \cdot (\rho \mathbf{v} \otimes \mathbf{v})$ and $\frac{\partial \rho \mathbf{v}}{\partial t}$ can be neglected. In this case one can derive the overdamped DDFT from (1) as [13, 29]

$$\begin{cases} \partial_t \rho(\boldsymbol{r};t) = \boldsymbol{\nabla}_{\boldsymbol{r}} \cdot \left[\boldsymbol{\Gamma}^{-1} \rho(\boldsymbol{r};t) \boldsymbol{\nabla}_{\mathbf{r}} \dfrac{\delta \mathcal{E}[\rho]}{\delta_{\mathbf{r}} \rho(\boldsymbol{r};t)} \right] & \mathbf{r} \in \mathbb{R}^d, \ t > 0, \\ \rho(\mathbf{r};0) = \rho_0(\mathbf{r}), \end{cases} \tag{2}$$

where $\mathcal{E}(\rho)$ denotes the free energy of the system which here is assumed to have the general form

$$\mathcal{E}(\rho) = \int_{\mathbb{R}^d} H(\rho) d\mathbf{r} + \int_{\mathbb{R}^d} V(\mathbf{r}) \rho \, d\mathbf{r} + \frac{1}{2} \int_{\mathbb{R}^d} (W(\mathbf{r}) \star \rho(\mathbf{r})) \rho(\mathbf{r}) \, d\mathbf{r}, \tag{3}$$

with $H(\rho)$ describing the dependency of the free energy $\mathcal{E}(\rho)$ on the local density field ρ, $V(\mathbf{r})$ accounting for the effects of external potentials and $W \star \rho$ accounting for the inter-particle potential. In the specific case of ideal-gas systems, the free-energy functional reduces to $E[\rho] = \int \rho \left(\log \rho - 1 \right) d\mathbf{r}$, with the typical entropic contribution $\rho \log \rho$. However, adopting a general energy functional allows us to model systems in the presence of various levels of complexity such as nonlinear diffusion, external potentials and non-local inter-particle interactions. Furthermore, the tensor $\boldsymbol{\Gamma}^{-1}$ is also assumed to be positive definite due to physical constraints and symmetric.

Gradient-flow equations such as (2) have an important property: their free energy $\mathcal{E}(\rho)$ decreases monotonically over time [30, 31]. For (2) this can be shown by taking time-derivative of the free energy:

$$\begin{aligned} \frac{d}{dt} E(\rho) &= \int_{\mathbb{R}^d} H'(\rho) \frac{\partial \rho}{\partial t} + V \frac{\partial \rho}{\partial t} + \frac{1}{2} ((W \star \frac{\partial \rho}{\partial t}) \rho + \frac{\partial \rho}{\partial t} (W \star \rho)) d\mathbf{r} \\ &= \int_{\mathbb{R}^d} (V + H'(\rho) + W \star \rho) \frac{\partial \rho}{\partial t} d\mathbf{r} \\ &= \int_{\mathbb{R}^d} (V + H'(\rho) + W \star \rho) \nabla \cdot (\boldsymbol{\Gamma}^{-1} \rho \nabla (H'(\rho) + V + W \star \rho)) d\mathbf{r} \\ &= - \int_{\mathbb{R}^d} \nabla (V + H'(\rho) + W * \rho)^T \boldsymbol{\Gamma}^{-1} \rho \nabla (V + H'(\rho) + W \star \rho) d\mathbf{r} \\ &= - \int_{\mathbb{R}^d} \rho \mathbf{v}^T \boldsymbol{\Gamma}^{-1} \mathbf{v} d\mathbf{r} < 0, \end{aligned} \tag{4}$$

where $\mathbf{v}$ can be interpreted as the velocity in the gradient flow (2) and satisfies $\mathbf{v} = -\nabla \left(H'(\rho) + V + W \star \rho \right)$.

The structure of (2) is similar to the gradient-flow equations considered in previous works [32, 33, 34, 35, 36, 37, 27, 38], but with the difference that in this work the diffusion parameter $\boldsymbol{\Gamma}^{-1}$ is considered, in general, non-constant in

space and time. For homogeneous diffusion, previous works have proposed several numerical schemes. For instance, Ref [33] developed a finite-volume scheme for degenerate parabolic equations with a density-dependent mobility. Carrillo and coworkers have proposed semi-discrete [34] and discrete [35] finite-volume schemes satisfying the decay of the discrete free energy. Other numerical strategies adopted to solve these kind of equations include finite-element schemes for nonlinear diffusion equations [32], discontinuous Galerkin [36] and the blob method [39, 40]. It is also worth mentioning that the overdamped DDFT equation in (2) does not require of well-balanced schemes to preserve stationary solutions, since there is no balance of sources and convective fluxes. On the contrary, the hydrodynamic system in (1) relies on well-balanced schemes to accurate evolve long-time solutions leading to stationary states [41, 42, 27].

Here we appropriately previous methodologies in the literature by developing a finite-volume scheme to solve gradient flow equations with non-homogeneous diffusion of the form (2), obtained in the framework of DDFT. The scheme allows us to study colloidal systems placed in non-homogeneous thermal baths and with a general free-energy functional accounting for external fields and inter-particle potentials. Specifically, we adopt a first- and second-order upwind approach for the space discretization in both one- and two-dimensional cases (1D and 2D, respectively). Moreover, we prove that our scheme satisfies the discrete analogy of the free-energy decay in (4), thanks to the upwind formulation. We exemplify our scheme through several case studies of systems with underlying thermal baths characterized by anisotropic, space-dependent and time-dependent properties. The main contributions of this work can be summarized as follows:

- Developing 1D and 2D finite-volume numerical schemes that preserve the non-negativity of the density if given CFL conditions are satisfied.
- Offering useful insight into the time evolution of the free energy for gradient flow equations [see for instance Figures 2(c), 3(c), 4(b), 7(g) and 9(i)]. The (monotonic) decay of the free energy is an important feature of deterministic gradient flow equations, such as DDFT, and we proved that the proposed schemes ensure a decay of the discrete free energy functional in 1D and 2D.
- Performing order-of-convergence analyses for both 1st and 2nd order schemes in 1D and 2D by running numerical simulations for a different number of cells (e.g. see Tables 1 and 2).
- Developing a methodology to simulate systems characterized by a range of free-energy functionals with space- or time-dependent diffusion, modelling relevant physical scenarios.

In Sect. 2, we discuss the numerical methodology of our finite-volume scheme for the 1D and 2D cases, detailing the construction of the first- and second-order schemes and relevant properties such as the positivity of the density and decay of the discrete free energy. Subsequently, in Sect. 3 we apply the numerical methodology we developed to several prototypical systems, including thermal baths with space- and time-dependent properties, emphasising also the differences in the dynamical evolution between homogeneous and non-homogeneous diffusion. Finally, conclusions and future developments are offered in Sect. 4.

2. Numerical methods

2.1. 1D scheme

The 1D version of the gradient-flow equation with non-homogeneous diffusion in (2) is

$$\partial_t \rho = \partial_x \left(\Gamma^{-1} \rho \partial_x \left(H'(\rho) + V + W \star \rho \right) \right), \tag{5}$$

where Γ^{-1} can be a positive number or a positive function depending on time t, space x and density ρ. The finite-volume formulation of (5) follows from dividing the computational domain $[0, L]$ in N cells $C_i = [x_{j-1/2}, x_{j+1/2}]$, all with uniform size $\Delta x = L/N$, so that the centre of the cell satisfies $x_j = (j-1)\Delta x/L + \Delta x/2$, $j \in \{1, \ldots, N\}$. In each of the cells we define the density cell average ρ_j as

$$\rho_j(t) = \frac{1}{\Delta x} \int_{C_j} \rho(x, t) dx.$$

Subsequently, one has to integrate equation (5) over each of the cells C_j which leads in the usual finite-volume discretization

$$\frac{d\rho_j}{dt} = -\frac{1}{\Delta x}(F_{j+1/2} - F_{j-1/2}), \tag{6}$$

where $F_{i\pm1/2}$ denote the numerical fluxes. Their evaluation follows an upwind approach inspired by the numerical scheme of Carrillo and coworkers [34],

$$F_{j+1/2} = u^+_{j+1/2}\rho_j + u^-_{j+1/2}\rho_{j+1}, \tag{7}$$

where the velocity $u_{i+1/2}$ satisfies

$$u_{j+1/2} = -\left(\Gamma^{-1}\right)_{j+1/2}\frac{\xi_{j+1} - \xi_j}{\Delta x}, \tag{8}$$

and the upwind approach is obtained with

$$u^+_{j+1/2} = \max(u_{j+1/2}, 0), \quad u^-_{j+1/2} = \min(u_{j+1/2}, 0). \tag{9}$$

The discretized variation of the free energy ξ_j is taken as

$$\xi_j = \Delta x \sum_l W(x_j - x_l)\rho_l + H'(\rho_j) + V(x_j). \tag{10}$$

The evaluation of $\left(\Gamma^{-1}\right)_{j+1/2}$ at the interface $x_{j+1/2}$ is obtained explicitly if Γ^{-1} depends only on x or t. Otherwise, if it depends on ρ, it is approximated as $\left(\Gamma^{-1}\right)_{j+1/2} = \left(\Gamma^{-1}(\rho_j) + \Gamma^{-1}(\rho_{j+1})\right)/2$.

The profile in each cell C_j is reconstructed as a constant for the first-order scheme, or as a linear function for the second-order scheme,

$$\widetilde{\rho}_j(x) = \begin{cases} \rho_j, & x \in C_i, \quad \text{for the first-order scheme,} \\ \rho_j + (\rho_x)_j(x - x_j), & x \in C_j, \quad \text{for the second-order scheme,} \end{cases} \tag{11}$$

so that the east and the west values ρ^E_j and ρ^W_j at the cell interfaces $x_{j+1/2}$ and $x_{j-1/2}$, respectively, are approximated as

$$\begin{cases} \rho^E_j = \rho_j, \quad \rho^W_j = \rho_j & \text{for the first-order scheme,} \\ \rho^E_j = \rho_j + \frac{\Delta x}{2}(\rho_x)_j, \quad \rho^W_j = \rho_j - \frac{\Delta x}{2}(\rho_x)_j & \text{for the second-order scheme.} \end{cases} \tag{12}$$

The numerical derivatives $(\rho_x)_j$ at every cell C_j are computed by means of an adaptive procedure which ensures that the point values (12) are second-order and nonnegative. This procedure initially takes centred apporximations of the form $(\rho_x)_j = \left(\rho_{j+1} - \rho_{j-1}\right)/(2\Delta x)$. Then, if it happens that $\rho^E_j < 0$ or $\rho^W_j < 0$, it employs a minmod limiter which ensures that the reconstructed values are nonnegative as far as the cell averages ρ_j are nonnegative,

$$(\rho_x)_j = \text{minmod}\left(\theta\frac{\rho_{j+1} - \rho_j}{\Delta x}, \frac{\rho_{j+1} - \rho_{j-1}}{2\Delta x}, \theta\frac{\rho_j - \rho_{j-1}}{\Delta x}\right),$$

where

$$\text{minmod}(z_1, z_2, \ldots) = \begin{cases} \min(z_1, z_2, \ldots), & \text{if } z_j > 0 \quad \forall j, \\ \max(z_1, z_2, \ldots), & \text{if } z_j < 0 \quad \forall j, \\ 0, & \text{otherwise.} \end{cases}$$

The parameter θ controls the numerical viscosity and it is taken to be $\theta = 2$.

The no-flux conditions are numerically implemented by taking the numerical flux (7) to be zero at the boundaries,

$$\begin{aligned} F^{n+1}_{j-1/2} &= 0 \text{ for } j = 1, \\ F^{n+1}_{j+1/2} &= 0 \text{ for } j = N, \end{aligned} \tag{13}$$

We conclude the construction of the finite-volume scheme by showing two properties related to the preservation of positivity for the density and decay of the discrete equivalent to the free energy in (3), defined as

$$E_\Delta(\rho) = \Delta x \sum_j \left(V_j\rho_j + H(\rho_j) + \frac{1}{2}\Delta x \sum_i W_{j-i}\rho_i\rho_j\right). \tag{14}$$

Theorem 2.1 (Positivity preserving). The semi-discrete finite-volume scheme (6)-(11), discretized in time by the forward Euler method or a higher-order ODE solver whose time step Δt can be expressed as a linear superposition of several forward Euler steps, preserves the positivity of the cell-averages $\rho_j \geq 0 \, \forall \, j$ if the following CFL condition is satisfied:

$$\begin{cases} \Delta t \leq \dfrac{\Delta x}{\max_j\{u^+_{j+1/2} - u^-_{j+1/2}\}} & \text{for the first-order reconstruction in (11);} \\ \Delta t \leq \dfrac{\Delta x}{2\max_j\{u^+_{j+1/2}, -u^-_{j+1/2}\}} & \text{for the second-order reconstruction in (11).} \end{cases}$$

Proof. The proof follows the same lines as in [34]. □

Theorem 2.2 (Discrete-energy decay). The semi-discrete finite-volume scheme (6)-(9), coupled with a positivity preserving reconstruction (11) for ρ, satisfies the following decay of the discrete free energy (22):

$$\frac{d}{dt}E_\Delta(t) \leq -I_\Delta(t), \tag{15}$$

where the discrete version of the entropy dissipation results in

$$I_\Delta(t) = \Delta x \sum_j \frac{\left(u_{j+1/2}\right)^2}{\left(\Gamma^{-1}\right)_{j+1/2}} \min_j\left(\rho_j, \rho_{j+1}\right). \tag{16}$$

Proof. The proof extends the one in [34] by taking into account the non-homogeneous diffusion Γ^{-1}. We begin by differentiating E_Δ in (22) with respect to time, and subsequently apply the finite-volume scheme (6):

$$\frac{d}{dt}E_\Delta = \Delta x \sum_j \left[V_j + H'\left(\rho_j\right) + \sum_i W_{j-i}\rho_j\right]\frac{d\rho_j}{dt} = -\Delta x \sum_j \xi_j \frac{F_{j+1/2} - F_{j-1/2}}{\Delta x}.$$

Then, by integrating by parts and applying (7)-(8) one gets:

$$\frac{d}{dt}E_\Delta = -\sum_j \left(\xi_j - \xi_{j+1}\right)F_{j+1/2} = -\Delta x \sum_j \frac{u_{j+1/2}}{\left(\Gamma^{-1}\right)_{j+1/2}}\left(u^+_{j+1/2}\rho_j + u^-_{j-1/2}\rho_{j+1}\right).$$

Finally, this last expression yields the negative upper bound in (15) with the entropy dissipation defined as in (16). □

2.2. 2D scheme

We proceed to describe the semi-discrete finite-volume formulation for the 2D version of equation (2). Note that for this 2D case the non-homogeneous diffusion $\mathbf{\Gamma}^{-1}$ is a 2×2 matrix which can depend on x, y, t and ρ. We assume that $\mathbf{\Gamma}^{-1}$ is symmetric and positive definite, and we denote its components as

$$\mathbf{\Gamma}^{-1} = \begin{pmatrix} a & b \\ b & c \end{pmatrix}. \tag{17}$$

We divide the computational domain in rectangular cells $C_{j,k} = [x_{j-1/2}, x_{j+1/2}]\times[y_{k-1/2}, y_{k+1/2}]$, which are assumed to have uniform size $\Delta x\,\Delta y$ so that $x_{j+1/2} - x_{j-1/2} = \Delta x, \ \forall \, j$, and $y_{k+1/2} - y_{k-1/2} = \Delta y, \ \forall k$. In each cell $C_{j,k}$ we define the density cell average as

$$\rho_{j,k}(t) = \frac{1}{\Delta x \Delta y}\int_{C_{j,k}} \rho(x, y, t)\, dx\, dy.$$

The finite-volume 2D formulation follows from first integrating equation (2) over each of the cells $C_{i,j}$, and subsequently applying the divergence theorem to get:

$$\frac{d\rho_{j,k}}{dt} = -\frac{F^x_{j+1/2,k} - F^x_{j-1/2,k}}{\Delta x} - \frac{F^y_{j,k+1/2} - F^y_{j,k-1/2}}{\Delta y}. \tag{18}$$

The numerical fluxes at the boundaries are obtained by an upwind approach as

$$F^x_{j+1/2,k} = u^+_{j+1/2,k}\rho^E_{j,k} + u^-_{j+1/2,k}\rho^W_{j+1,k}, \quad F^y_{j,k+1/2} = v^+_{j,k+1/2}\rho^N_{j,k} + v^-_{j,k+1/2}\rho^S_{j,k+1}, \tag{19}$$

where the velocities now satisfy

$$\begin{aligned} u_{j+1/2,k} &= -a_{j+1/2,k}\left(\frac{\xi_{j+1,k}-\xi_{j,k}}{\Delta x}\right) - b_{j+1/2,k}\left(\frac{\xi_{j,k+1}-\xi_{j,k}}{\Delta y}\right), \\ v_{j,k+1/2} &= -b_{j,k+1/2}\left(\frac{\xi_{j+1,k}-\xi_{j,k}}{\Delta x}\right) - c_{j,k+1/2}\left(\frac{\xi_{j,k+1}-\xi_{j,k}}{\Delta y}\right), \end{aligned} \tag{20}$$

due to the dimensional coupling through the non-homogeneous diffusion $\mathbf{\Gamma}^{-1}$ in (17). The upwind approach is accomplished by

$$\begin{aligned} \left(u_{j+1/2,k}\right)^+ &= \max\left(u_{j+1/2,k},0\right), \quad \left(u_{j+1/2,k}\right)^- = \min\left(u_{j+1/2,k},0\right), \\ \left(v_{j,k+1/2}\right)^+ &= \max\left(v_{j,k+1/2},0\right), \quad \left(v_{j,k+1/2}\right)^- = \min\left(v_{j,k+1/2},0\right). \end{aligned} \tag{21}$$

The discretized variation of the free energy $\xi_{j,k}$ is taken as

$$\xi_{j,k} = \Delta x\Delta y \sum_{l,m} W(x_j - x_l, y_k - y_m)\rho_{l,m} + H'(\rho_{j,k}) + V(x_j, y_k). \tag{22}$$

The reconstructions of the density at the sides of the cells are denoted as $\rho^E_{j,k}, \rho^W_{j,k}, \rho^N_{j,k}$ and $\rho^S_{j,k}$. They are computed by means of a first- or second-order reconstruction of the form

$$\begin{cases} \rho^E_{j,k} = \rho_{j,k}, \quad \rho^W_{j,k} = \rho_{j,k}, & \text{for the first-order scheme,} \\ \rho^E_{j,k} = \rho_{j,k} + \frac{\Delta x}{2}(\rho_x)_{j,k}, \quad \rho^W_{j,k} = \rho_{j,k} - \frac{\Delta x}{2}(\rho_x)_{j,k}, & \text{for the second-order scheme,} \end{cases} \tag{23}$$

for $\rho^E_{j,k}$ and for $\rho^W_{j,k}$, and of the form

$$\begin{cases} \rho^N_{j,k} = \rho_{j,k}, \quad \rho^S_{j,k} = \rho_{j,k}, & \text{for the first-order scheme,} \\ \rho^N_{j,k} = \rho_{j,k} + \frac{\Delta y}{2}\left(\rho_y\right)_{j,k}, \quad \rho^S_{j,k} = \rho_{j,k} - \frac{\Delta y}{2}\left(\rho_y\right)_{j,k}, & \text{for the second-order scheme,} \end{cases} \tag{24}$$

for $\rho^N_{j,k}$ and for $\rho^S_{j,k}$. As with the 1D set up, the slopes are initially computed by means of central-difference approximations satisfying

$$(\rho_x)_{j,k} = \frac{\rho_{j+1,k}-\rho_{j,k}}{2\Delta x} \quad \text{and} \quad \left(\rho_y\right)_{j,k} = \frac{\rho_{j,k+1}-\rho_{j,k}}{2\Delta y}. \tag{25}$$

If at any point in the time evolution the reconstructions become negative, we recompute the slopes $(\rho_x)_{j,k}$ and $(\rho_y)_{j,k}$ by means of a monotone nonlinear limiter which ensures nonnegativity. Following Ref. [34], we apply the generalized mimmod limiters with $\theta \in [1,2]$:

$$\begin{aligned} (\rho_x)_{j,k} &= \text{minmod}\left(\theta\frac{\rho_{j+1,k}-\rho_{j,k}}{\Delta x}, \frac{\rho_{j+1,k}-\rho_{j-1,k}}{2\Delta x}, \theta\frac{\rho_{j,k}-\rho_{j-1,k}}{\Delta x}\right), \\ \left(\rho_y\right)_{j,k} &= \text{minmod}\left(\theta\frac{\rho_{j,k+1}-\rho_{j,k}}{\Delta y}, \frac{\rho_{j,k+1}-\rho_{j,k-1}}{2\Delta y}, \theta\frac{\rho_{j,k}-\rho_{j,k-1}}{\Delta y}\right). \end{aligned} \tag{26}$$

The numerical no-flux conditions are implemented by taking the numerical flux (19) to be zero at the boundaries:

$$\begin{aligned} F^x_{j-\frac{1}{2},k} &= 0 \text{ for } j = 1, \forall k, \quad F^x_{j+\frac{1}{2},k} = 0 \text{ for } j = N, \forall k, \\ F^y_{j,k-\frac{1}{2}} &= 0 \text{ for } k = 1, \forall j; \quad F^y_{j,k+\frac{1}{2}} = 0 \text{ for } k = N, \forall j. \end{aligned} \tag{27}$$

We conclude this subsection by proving the 2D version of the positivity of the density and the decay of the discrete free energy.

Theorem 2.3 (Positivity preserving). The 2D semi-discrete finite-volume scheme (18)-(22), coupled with a positivity preserving reconstruction (23)-(24) for ρ, and discretized in time by the forward Euler method or a higher-order ODE solver whose time step Δt can be expressed as a linear superposition of several forward Euler steps, preserves the positivity of the cell-averages $\rho_{j,k} \geq 0 \; \forall \{j,k\}$ if the following CFL condition is satisfied:

$$\begin{cases} \Delta t \leq \min_{i,j} \left\{ \dfrac{u^+_{j+1/2,k} - u^-_{j-1/2,k}}{\Delta x} + \dfrac{v^+_{j,k+1/2} - v^-_{j,k-1/2}}{\Delta y} \right\} & \text{for the first-order reconstruction in (23)-(24);} \\ \Delta t \leq \min_{i,j} \left\{ \dfrac{\Delta x}{4 \max\left\{u^+_{j+1/2,k}, u^-_{j+1/2,k}\right\}}, \dfrac{\Delta y}{4 \max\left\{v^+_{j,k+1/2}, v^-_{j,k+1/2}\right\}} \right\} & \text{for the second-order reconstruction in (23)-(24).} \end{cases}$$

Proof. The proof follows the same lines as in [34]. For the second-order scheme it follows that

$$\begin{aligned} \rho_{j,k}(t+\Delta t) &= \rho_{j,k}(t) + \Delta t \left(- \frac{F^x_{j+1/2,k} - F^x_{j-1/2,k}}{\Delta x} - \frac{F^y_{j,k+1/2} - F^y_{j,k-1/2}}{\Delta y} \right) \\ &= \frac{1}{4}\left(\rho^E_{j,k} + \rho^W_{j,k} + \rho^N_{j,k} + \rho^S_{j,k}\right) - \Delta t \left(\frac{1}{\Delta x} \left(u^+_{j+1/2,k} \rho^E_{j,k} + u^-_{j+1/2,k} \rho^W_{j+1,k} - u^+_{j-1/2,k} \rho^E_{j-1,k} - u^-_{j-1/2,k} \rho^W_{j,k} \right) \right) \\ &- \Delta t \left(\frac{1}{\Delta y} \left(v^+_{j,k+1/2} \rho^N_{j,k} + v^-_{j,k+1/2} \rho^S_{j,k+1} - v^+_{j,k-1/2} \rho^N_{j,k-1} - v^-_{j,k-1/2} \rho^S_{j,k} \right) \right) \\ &= \left(\frac{1}{4} - \frac{\Delta t}{\Delta x} u^+_{j+1/2,k} \right) \rho^E_{j,k} + \left(\frac{1}{4} + \frac{\Delta t}{\Delta x} u^-_{j+1/2,k} \right) \rho^W_{j,k} + \left(\frac{1}{4} - \frac{\Delta t}{\Delta y} v^+_{j,k+1/2} \right) \rho^N_{j,k} + \left(\frac{1}{4} + \frac{\Delta t}{\Delta y} v^-_{j,k+1/2} \right) \rho^S_{j,k} \\ &- \frac{\Delta t}{\Delta x} u^-_{j+1/2,k} \rho^W_{j+1,k} + \frac{\Delta t}{\Delta x} u^+_{j-1/2,k} \rho^E_{j-1,k} - \frac{\Delta t}{\Delta y} v^-_{j,k+1/2} \rho^S_{j,k+1} + \frac{\Delta t}{\Delta y} v^+_{j,k-1/2} \rho^N_{j,k-1} \end{aligned}$$

Since the reconstructed point values $\rho^E_{j,k}$, $\rho^W_{j,k}$, $\rho^N_{j,k}$, $\rho^S_{j,k}$ are nonnegative and $u^+_{j+1/2,k} \geq 0$, $u^-_{j+1/2,k} \leq 0$, $v^+_{j,k+1/2} \geq 0$, $v^-_{j,k+1/2} \leq 0$, we deduce the CFL condition ensuring $\rho_{j,k}(t+\Delta t) \geq 0 \; \forall j,k$. The proof of the first-order CFL condition can be derived similarly.

□

Remark 2.1 (Diagonalization of Γ^{-1} before proving decay of discrete free energy). For the decay of the discrete free energy it is important to note that a full Γ^{-1} matrix (17) where $b \neq 0$ produces a dimensional coupling in the gradient flow (2), since the velocities (20) now contain terms from orthogonal directions. This can be avoided by performing a diagonalization of the matrix Γ^{-1}, which is ensured due to the conditions imposed over it (namely that it is symmetric and positive definite). To show this we can first diagonalize Γ^{-1} as

$$\Gamma^{-1} = QDQ^T,$$

where $QQ^T = Id_2$ and D is a positive diagonal matrix

$$D = \begin{bmatrix} \alpha & 0 \\ 0 & \beta \end{bmatrix}.$$

Formally, we can project the gradient operator onto the eigenvectors basis: $\nabla = Q\nabla_e$, and $\nabla \cdot F = \nabla^T F = \nabla_e^T (Q^T F) = \nabla_e \cdot (Q^T F)$. Therefore, the gradient-flow equation in (2) becomes

$$\frac{\partial \rho}{\partial t} = (Q\nabla_e)^T \left(QDQ^T Q \nabla_e \frac{\delta \mathcal{E}[\rho]}{\delta \rho} \right) = (Q\nabla_e)^T \left(QD\nabla_e \frac{\delta \mathcal{E}[\rho]}{\delta \rho} \right) = \nabla^T \left(D\nabla_e \frac{\delta \mathcal{E}[\rho]}{\delta \rho} \right),$$

so that (2) can now be written in the eigenvector basis as,

$$\frac{\partial \rho}{\partial t} = \nabla_e \cdot (D \nabla_e \rho). \tag{28}$$

The advantage of this formulation is that for (28) the diffusion matrix D is diagonal which then simplifies the velocities in (20) since $b = 0$. Following this transformation one can then show the decay of the discrete free energy for (28). Such discrete energy comes from the general free energy (3) and its 2D version satisfies:

$$E_\Delta = \Delta x \Delta y \sum_{j,k} V_{j,k}\,\rho_{j,k} + H(\rho_{j,k}) + \frac{1}{2}\Delta x \Delta y \sum_{l,m} W_{j-l,k-m}\,\rho_{l,m}\,\rho_{j,k}. \tag{29}$$

Theorem 2.4 (Decay of discrete free energy). The 2D semi-discrete finite-volume scheme (18)-(22), coupled with a positivity preserving reconstruction (23)-(24) for ρ, satisfies the following decay of the discrete free energy (29) for gradient flows where $b = 0$ in $\mathbf{\Gamma}^{-1}$ (17) or previously diagonalized as in (28):

$$\frac{d}{dt}E_\Delta(t) \leq -I_\Delta(t), \tag{30}$$

where the discrete version of the entropy dissipation results in

$$I_\Delta(t) = -\Delta x \Delta y \sum_{j,k} \left[\frac{\left(u_{j+1/2,k}\right)^2}{a_{j+1/2,k}} + \frac{\left(v_{j,k+1/2}\right)^2}{c_{j,k+1/2}} \right] \min_{j,k} \left(\rho^E_{j,k}, \rho^W_{j+1,k}, \rho^N_{j,k}, \rho^S_{j,k+1}\right). \tag{31}$$

Proof. Following the 1D proof in subsection 2.1, the temporal decay of the discrete free energy in (29) yields

$$\frac{d}{dt}E_\Delta(t) = -\Delta x \Delta y \sum_{j,k} \xi_{j,k} \left(\frac{F^x_{j+1/2,k} - F^x_{j-1/2,k}}{\Delta x} + \frac{F^y_{j,k+1/2} - F^y_{j,k-1/2}}{\Delta y} \right).$$

Then, by applying integration by parts with respect to both x and y yields:

$$\frac{d}{dt}E_\Delta(t) = -\Delta x \Delta y \sum_{j,k} \left[\left(\frac{\xi_{j,k} - \xi_{j+1,k}}{\Delta x} \right) F^x_{j+1/2,k} + \left(\frac{\xi_{j,k} - \xi_{j,k+1}}{\Delta y} \right) F^y_{j,k+1/2} \right).$$

With $b = 0$ in $\mathbf{\Gamma}^{-1}$ (17) and the expressions for the velocities in (20) and the fluxes in (19), it follows that:

$$\begin{aligned}
\frac{d}{dt}E_\Delta(t) &= -\Delta x \Delta y \sum_{j,k} \left[\frac{u_{j+1/2,k}}{a_{j+1/2,k}} \left(u^+_{j+1/2,k}\rho^E_{j,k} + u^-_{j+1/2,k}\rho^W_{j+1,k} \right) + \frac{v_{j,k+1/2}}{c_{j,k+1/2}} \left(v^+_{j,k+1/2}\rho^N_{j,k} + v^-_{j,k+1/2}\rho^S_{j,k+1} \right) \right] \\
&\leq -\Delta x \Delta y \sum_{j,k} \left[\frac{\left(u_{j+1/2,k}\right)^2}{a_{j+1/2,k}} + \frac{\left(v_{j,k+1/2}\right)^2}{c_{j,k+1/2}} \right] \min_{j,k} \left(\rho^E_{j,k}, \rho^W_{j+1,k}, \rho^N_{j,k}, \rho^S_{j,k+1}\right).
\end{aligned}$$

Thus, the decay of the discrete free energy in (30) is satisfied with a discrete entropy dissipation of the form (31). □

3. Numerical experiments

Here we present various numerical experiments for different test cases. The aim is to show the impact of a variable coefficient Γ^{-1} on the dynamical evolution of the solutions, as opposed to a constant Γ^{-1}.

The boundary conditions in all simulations are taken as no-flux and the temporal integrator scheme is the third order TVD Runge-Kutta method [43]. Notice that the TVD Runge-Kutta is a linear superposition of several forward Euler steps, and as a result the positivity and decay of discrete free energy still hold.

In subsection 3.1 we present 1D results, including an order-of-convergence study to show the first- and second-order spatial accuracy of the algorithms developed in section 2. Subsequently, subsection 3.2 deals with 2D relevant examples.

3.1. 1D case studies

We introduce in (2) nonhomogeneous diffusion functions Γ^{-1} which depend on space and time.

3.1.1. Order of convergence

The aim is to numerically test the convergence of the first- and second-order schemes presented in section 2. For this purpose we adopt the following model problem:

$$\frac{\partial \rho}{\partial t} = \frac{\partial}{\partial x}\left(\Gamma^{-1}\rho\frac{\partial}{\partial x}\left(\log(\rho) + V\right)\right), \tag{32}$$

where $V(x) = \frac{x^2}{2}$. The objective is to show the convergence both for a constant $\Gamma^{-1} = 1$ and for a non-homogeneous diffusion with a spatial dependency of the form $\Gamma^{-1}(x) = (1 + x/10)^{-1}$.

The computationnal domain is $[-5, 5]$ and we choose a Gaussian initial condition

$$\rho_0(x) = \frac{M}{\sqrt{2\pi\sigma^2}}\exp\left(-\frac{x^2}{2\sigma^2}\right)$$

with $M = 0.1$ and $\sigma = 0.3$.

The order-of-convergence analysis is performed by running the numerical simulation for different number of cells, each of them being twice the one of the previous simulation. Hence, the cell size Δx is halved after each run. We take 25, 50, 100, 200 and 400 cells. We then compute the L^1 error of the numerical solution $\rho_{\Delta x}$ at the final time of $t_f = 0.1$:

$$\epsilon(\Delta x) = \|\rho_{\Delta x}(x, t_f) - \rho^*(x, t_f)\|_{L^1},$$

where ρ^* is an approximate exact solution computed using a rather refined mesh 25600 cells. This is due to the lack of an explicit solution in time for (32).

Once the errors are computed, the order of convergence is obtained from:

$$o(\Delta x) = \log_2\left(\frac{\epsilon(\Delta x)}{\epsilon\left(\frac{\Delta x}{2}\right)}\right).$$

Our results for the homogeneous diffusion with $\Gamma^{-1} = 1$ are depicted in table 1, while the ones for $\Gamma^{-1}(x) = (1 + x/10)^{-1}$ are shown in table 2. They clearly indicate the first- and second-order convergence for the numerical schemes we developed in section 2.

Table 1: Accuracy test for $\Gamma^{-1} = 1$ with the first and second-order schemes

Number of cells	First-order		Second-order	
	L^1 error	order	L^1 error	order
25	6.6799E-04	-	2.1809E-04	-
50	4.5326E-04	0.56	1.5584E-04	0.48
100	2.4109E-04	0.91	3.1933E-05	2.28
200	1.2539E-04	0.94	9.2375E-06	1.79
400	6.3969E-05	0.97	2.5768E-05	1.84

Table 2: Accuracy test for $\Gamma^{-1}(x) = (1 + x/10)^{-1}$ with the first and second-order schemes

Number of cells	First-order		Second-order	
	L^1 error	order	L^1 error	order
25	7.6616E-04	-	2.0353E-04	-
50	2.7646E-04	1.47	1.0347E-04	0.98
100	1.4445E-04	0.94	3.4502E-05	1.58
200	7.4119E-05	0.96	8.9064E-06	1.95
400	3.7201E-05	0.99	2.3364E-06	1.93

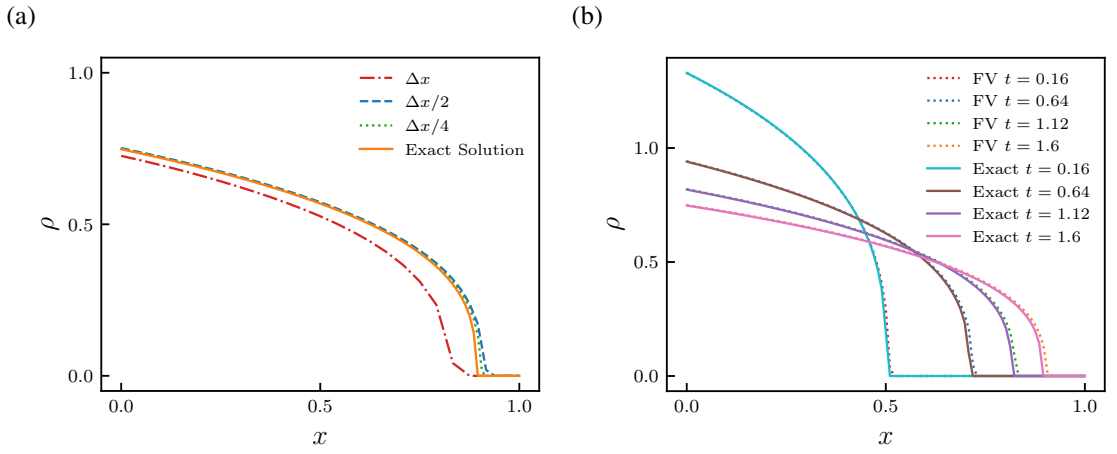

Fig. 1: (a) Convergence towards the exact solution for (34) at the final computational time $t = 1.6$sec; (b) Comparison between the finite-volume (FV) scheme and the exact solution. Parameter values: $M_\infty = 0.5$, $a = 1$, $b = 3$, $D_0 = 1$, $r_0 = 0.1$, $\Delta x = 0.042$ in (a) and $\Delta x = 0.01$ in (b).

3.1.2. Nonlinear diffusion equation in a radially symmetric inhomogeneous medium

This example is taken from [44]. Consider the following ν-dimensional nonlinear diffusion equation in polar coordinates:

$$\begin{cases} \dfrac{\partial \rho}{\partial t} = \dfrac{1}{r^{\nu-1}} \dfrac{\partial}{\partial r}(r^{\nu-1} D \dfrac{\partial \rho}{\partial r}), \\ \int_0^{r_0} \omega_\nu r^{\nu-1} \rho(r,0) dr = M_\infty, \\ J_\infty(0,t) = 0, \quad t > 0, \\ \rho(r,t) \to 0, \quad r \to \infty, \quad t > 0, \end{cases} \tag{33}$$

where r is the radius $r = \|\mathbf{x}\|$, $D(r,\rho) = D_0 r^a \rho^b$ is the diffusion coefficient ($0 < a < 2$, $b > 0$), $J_\infty(r,t) = -\omega_\nu D r^{\nu-1} \frac{\partial \rho}{\partial r}$ is the diffusive flux. This problem describes the evolution of an initial distribution of a diffusing substance. In [44], an analytical solution is derived,

$$\rho(r,t) = \begin{cases} C_0(t) \left[1 - \left(\frac{r}{r_f(t)} \right)^{2-a} \right]^{\frac{1}{b}} & \text{if} \quad r < r_f(t), \\ 0 & \text{otherwise}, \end{cases} \tag{34}$$

where $C_0(t)$ is the solution at the origin $r = 0$ and satisfies

$$C_0(t) \omega_\nu (r_f(t))^\nu I = M_\infty, \quad \text{with} \quad I = \int_0^1 s^{\nu-1} (1 - s^{2-a})^{\frac{1}{b}} ds, \tag{35}$$

and the front position $r_f(t)$ follows from

$$r_f(t) = \left[\frac{(2-a)^{b+1} (2 - a + b\nu) M_\infty^b D_0 (t + t_0)}{b \omega_\nu^b B^b} \right]^{\frac{1}{2-a+\nu b}}, \quad \text{with} \quad t_0 = \frac{b \omega_\nu^b r_0^{2-a+\nu b} B^b}{(2-a)^{b+1} (2 - a + \nu b) D_0 M_\infty^b}$$

and $B = \beta(\frac{\nu}{2-a}, \frac{b+1}{b})$, where the β-function satisfies:

$$\beta(u,v) = \int_0^1 t^{u-1} (1-t)^{v-1} dt.$$

In the 1D scenario we have that $r = |x|$, $\nu = 1$ and $\omega_\nu = 1$. We can then re-formulate the problem as:

$$\frac{\partial \rho}{\partial t} = \frac{\partial}{\partial r} \left(D_0 r^a \rho \frac{\partial}{\partial r} \left(\frac{\rho^b}{b} \right) \right). \tag{36}$$

Equation (36) is a particular case of (5) with $\Gamma^{-1}(r) = D_0 r^a$, $H'(\rho) = \dfrac{\rho^b}{b}$, $V = 0$ and $W = 0$. The conditions in (33) can be considered as Dirichlet ($\rho(r,t) \to 0$ when $r \to \infty$) and Neumann ($J_\infty(0,t) = 0$). The mass conservation is ensured due to the nature of the finite-volume schemes.

The results for this example are displayed in Figure 1. Figure 1 (a) depicts the convergence towards the exact solution (34). We notice how the discontinuous derivative at the front prevents the numerical solution for larger Δx to approach the exact solution. But as the mesh is refined the numerical solution converges to the exact one. On the other hand, Figure 1 (b) plots the numerical solution at different times comparing to the exact solution (34). Evidently the radial diffusion enlarges the compact support of the solution in time making the front advance.

3.1.3. Addition of an external field and a space-dependent diffusion coefficient

The aim of this example is to compare the temporal evolution of a constant and a space-dependent Γ^{-1}. For this we select the following model system:

$$\frac{\partial \rho}{\partial t} = \frac{\partial}{\partial x}\left(\Gamma^{-1}\rho\frac{\partial}{\partial x}\left(\nu\rho^{m-1} + V(x)\right)\right), \tag{37}$$

with an external potential satisfying $V(x) = \frac{x^4}{4} - \frac{x^2}{2}$ and $m = 3$ leading to compactly-supported densities. The simulations are performed on the domain $[-3,3]$, with $\Delta x = 0.06$ and $\nu = 1.48$. $\Gamma^{-1} = 1$ in the first example and $\Gamma^{-1}(x) = \chi_{x<0} + 0.5$ in the second. The first case is also investigated in [34]. The initial condition for the simulation is taken as:

$$\rho_0(x) = \frac{M}{\sqrt{2\pi\sigma^2}} e^{-\frac{x^2}{2\sigma^2}}, \quad M = 0.1, \quad \sigma^2 = 0.2.$$

The results comparing the constant and the space-dependent Γ^{-1} are shown in Figure 2. First, Figure 2 (a) reveals that for a constant Γ^{-1} the solution remains symmetric in time and two compactly-supported peaks are formed in the steady state due to the shape of the external potential $V(x)$. This agrees with the steady-state solution of equation (37) for $\Gamma^{-1} = 1$, which satisfies [34]

$$\rho_\infty(x) = \left(\frac{C(x) - V(x)}{\nu}\right)_+^{\frac{1}{m-1}},$$

with $C(x)$ being in this case piecewise constant due to the initial symmetric density.

Figure 2 (b) plots the time evolution for $\Gamma^{-1}(x) = \chi_{x<0} + 0.5$. Even though an asymmetric solution is observed during the temporal evolution, eventually the steady state approaches the case $\Gamma^{-1} = 1$. It should be noted that evolution on the left of the domain is faster due to the higher diffusion value of $\Gamma^{-1}(x)$ in that part of the domain.

Finally, in Figure 2 (c) we show how the discrete free energy (22) decreases in time for the two choices of Γ^{-1}. The space-dependent Γ^{-1} has a faster time convergence towards the steady state than the constant Γ^{-1}.

3.1.4. Nonlinear diffusion with non local attraction kernel

For this example we compare again the temporal evolution for both a constant and a space-dependent Γ^{-1}, as in the previous example. However, here we adopt the following model:

$$\frac{\partial \rho}{\partial t} = \frac{\partial}{\partial x}\left(\Gamma^{-1}\rho\frac{\partial}{\partial x}\left(\nu\rho^{m-1} + W(x) \star \rho\right)\right). \tag{38}$$

This equation models the competition between nonlinear diffusion and non-local attraction. The simulations are performed on the domain $[-3,3]$, with $\Delta x = 0.08$ and $\nu = 0.5$. $\Gamma^{-1} = 1$ in the first example and $\Gamma^{-1}(x) = \chi_{x<0} + 1$ in the second. The first case is also investigated in [34]. The initial condition for the simulation is taken as $\rho_0(x) = \chi_{[-1.5,1.5]}/4$.

The numerical results for this example are displayed in Figure 3. Figure 3 (a) shows the results for constant Γ^{-1}. We observe that initially two identical bumps are formed but they eventually merge into a single one when reaching the steady state. We notice that the solution remains symmetric for all times. Figure 3 (b) plots the time evolution for the space-dependent Γ^{-1}. We observe that the dynamics are similar to 3 (a), but here the two bumps are no longer symmetric. The diffusion coefficient on the left of the domain is larger than that on the right, and as a consequence the evolution is slower on the right. After a long time we recover the steady state of 3 (a).

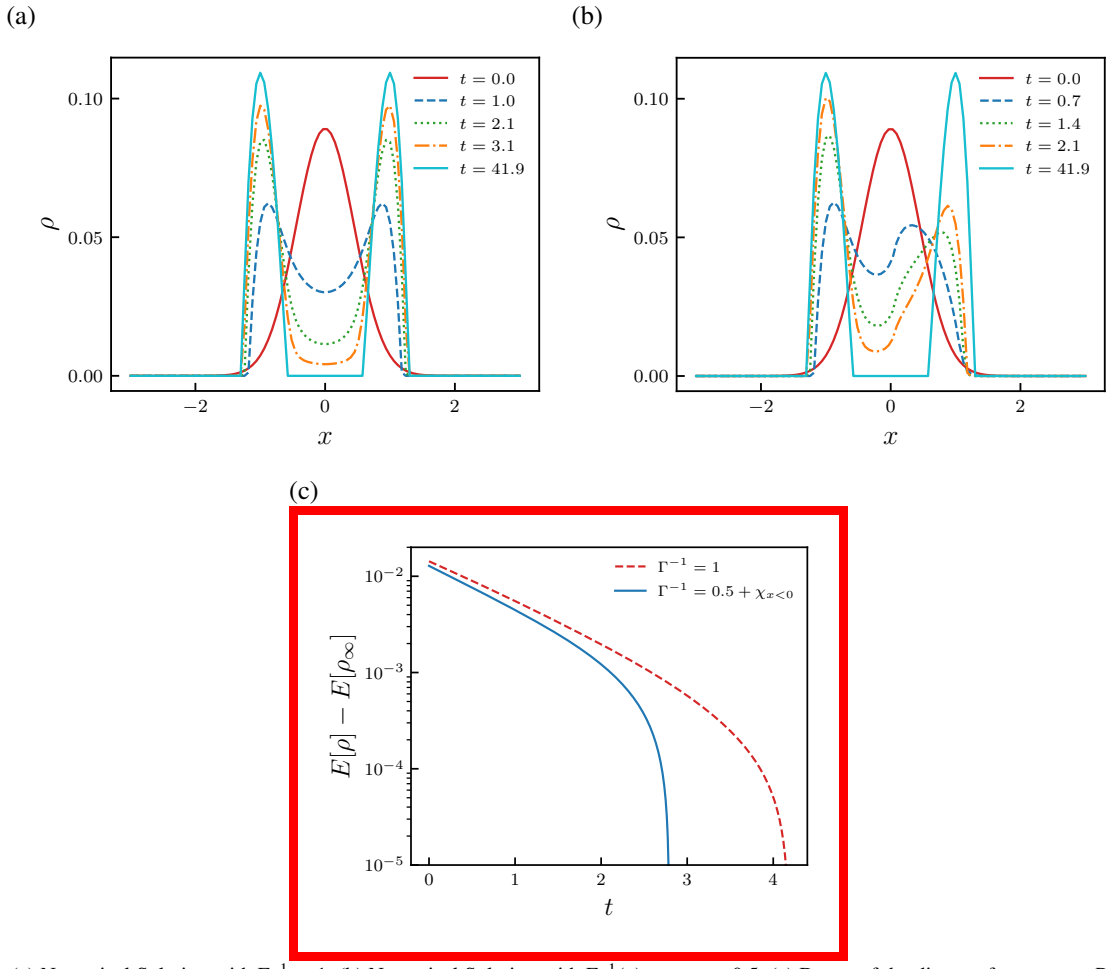

Fig. 2: (a) Numerical Solution with $\Gamma^{-1} = 1$, (b) Numerical Solution with $\Gamma^{-1}(x) = \chi_{x<0} + 0.5$, (c) Decay of the discrete free energy. Parameters values: $\nu = 1.48$, $m = 3$, $V(x) = \frac{x^4}{4} - \frac{x^2}{2}$ $\Delta x = 0.06$.

Finally, Figure 3 (c) depicts the decay in the discrete free energy computed as in (22). We notice the the faster time convergence of the solution for the case of space-dependent Γ^{-1}. Moreover, for $\Gamma^{-1} = 1$ two characteristic intermediate asymptotic behaviors are observed corresponding to straight lines: the first one corresponds to the merging of the two bumps, and the second to the formation of a single cluster of mass. For the case of space-dependent Γ^{-1} the free energy has only one intermediate exponential decays, and the overall evolution is faster.

3.1.5. Time-dependent diffusion coefficient $\Gamma^{-1}(t)$

Here we study the heat equation with a time-dependent diffusion:

$$\frac{\partial \rho}{\partial t} = \frac{\partial}{\partial x}\left(\Gamma^{-1}\frac{\partial}{\partial x}(\rho)\right), \tag{39}$$

where the following time-dependent diffusion coefficient Γ^{-1} is adopted:

$$\Gamma^{-1}(t) = \begin{cases} 1 & \text{if} \quad \cos(2\pi t) > 0.5, \\ 0 & \text{otherwise.} \end{cases}$$

The initial density for the simulations is $\rho_0(x) = \frac{1}{\sqrt{2\pi}} e^{-\frac{x^2}{2}}$, the spatial domain is $[-3, 3]$ and $\Delta x = 0.06$.

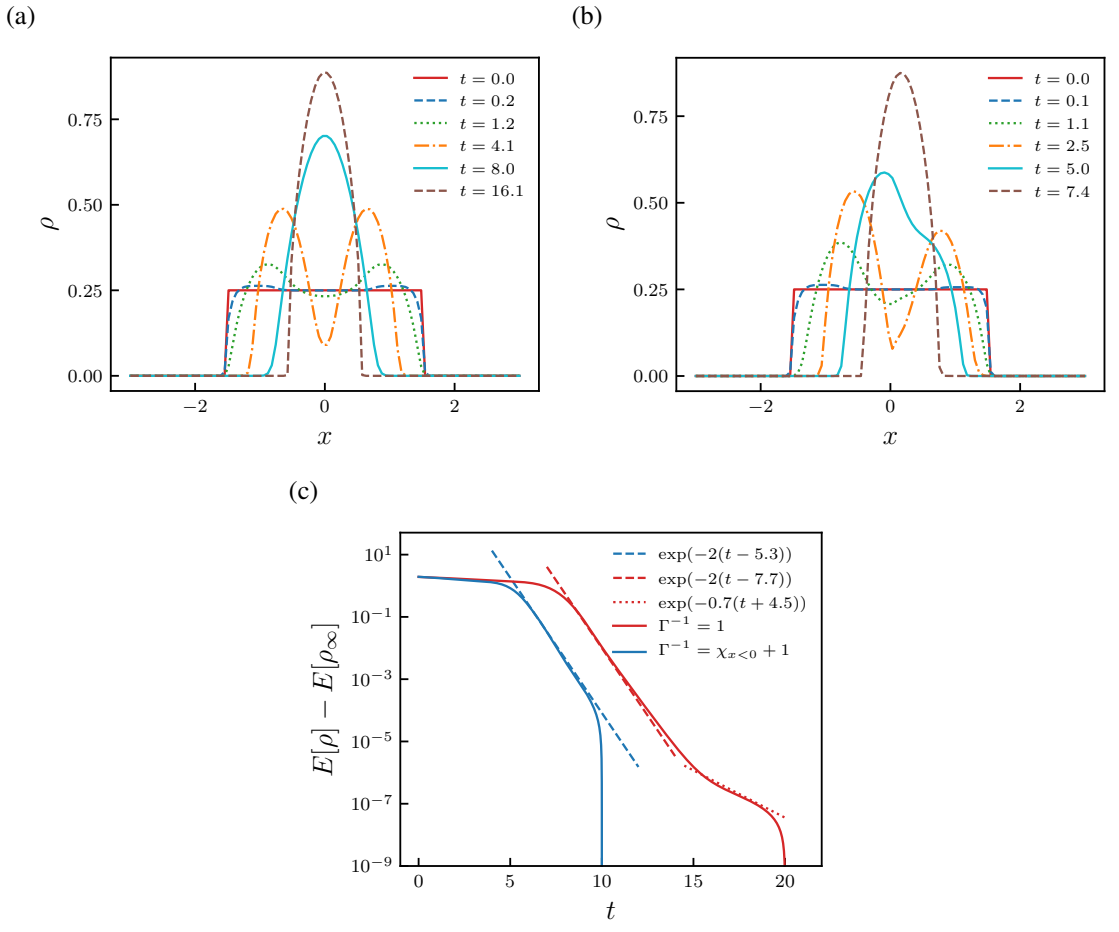

Fig. 3: (a) Numerical Solution with $\Gamma^{-1} = 1$, (b) Numerical Solution with $\Gamma^{-1}(x) = 1 + \chi_{x<0}$, (c) Decay of the discrete free energy. Parameter values: $\nu = 0.5$, $m = 3$, $W(x) = -(1 - |x|)\chi_{|x|<1}$,$\Delta x = 0.08$.

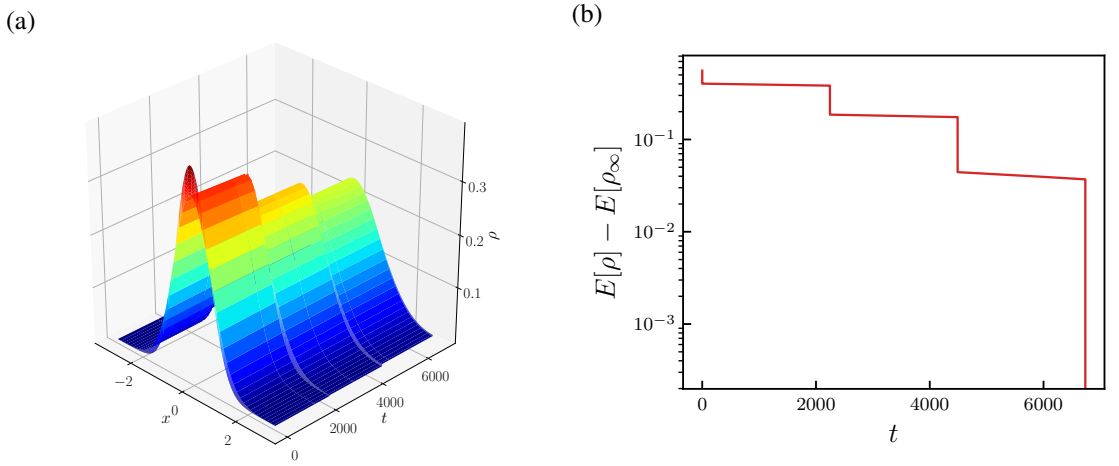

Fig. 4: Heat equation with a time-dependent diffusion Γ^{-1}. (a) Three-dimensional plot of the numerical solution, (b) Decay of the discrete free energy.

The results are shown in Figure 4. We notice a discontinuous time evolution which we explain by decomposing the evolution into certain time intervals. Consider I a union of intervals I_p such that $\forall t \in I : \Gamma^{-1}(t) = 1$. The problem at hand varies according to the time interval. For $t \in I_p =: [t_{2p}, t_{2p+1}]$, the problem the classical heat equation with the usual diffusion evolution. For $t \notin I$, we have a stationary problem: $\frac{\partial \rho}{\partial t} = 0 \quad \forall t \in [t_{2p+1}, t_{2p+2}]$. In this case $\rho(x,t) = \rho(x, t_{2p+1}) \quad \forall t \in [t_{2p+1}, t_{2p+2}]$. The free-energy plot in Figure 4 (b) confirms this discontinuous time evolution, observing also the free-energy decay in time.

3.2. 2D case studies

Here we present 2D examples. Here $\mathbf{\Gamma}^{-1}$ in (2) is a 2×2 matrix with space dependency.

3.2.1. Γ^{-1} constant matrix and order of convergence

Consider first a constant $\mathbf{\Gamma}^{-1}$ matrix, both with a diagonal form and as a full symmetric matrix. We take the following anisotropic diffusion problem:

$$\frac{\partial \rho}{\partial t} = \nabla \cdot (\mathbf{\Gamma}^{-1} \nabla \rho) \quad on \quad \Omega = [-A, A]^2. \tag{40}$$

An analytical solution of (40) can be obtained by means of 2D Fourier series. Suppose that the solution is periodic in space for all time. We can write its Fourier expansion as:

$$\rho(x, y, t) = \sum_{k,l} C_{k,l}(t) e^{i \frac{\pi}{A}(kx+ly)}.$$

The Fourier Coefficients of ρ satisfy:

$$\frac{dC_{k,l}}{dt}(t) = -\left(\frac{\pi}{A}\right)^2 \alpha_{k,l} C_{k,l}(t), \tag{41}$$

with $\alpha_{k,l} = ((\mathbf{\Gamma}^{-1})^T (k,l)^T).((k,l)^T)$.

Therefore $C_{k,l}(t) = C_{k,l}(0) \exp\left(-\left(\frac{\pi}{A}\right)^2 \alpha_{k,l} t\right)$. The coefficients $C_{k,l}(0)$ are the Fourier coefficients of the initial condition. To ensure the decrease of the Fourier coefficients, $\mathbf{\Gamma}^{-1}$ must be positive definite (ie: $\alpha_{k,l} > 0$ for $(k,l) \neq (0,0)$). In this case, we can approximate ρ with a truncated Fourier series:

$$\rho(x, y, t) \approx \sum_{|k|+|l| \leq N} C_{k,l}(t) e^{i \frac{\pi}{A}(kx+ly)}.$$

For this example we aim to compare the numerical simulation of (40) with the approximated exact solution from the truncated Fourier series. This example also serves to validate the order of convergence of the 2D scheme, similarly as in tables 1 and 2 for the 1D scheme. For this purpose we take the following two $\mathbf{\Gamma}$ matrices:

$$\mathbf{\Gamma_1} = \begin{bmatrix} 10 & 0 \\ 0 & 1 \end{bmatrix}, \quad \mathbf{\Gamma_2} = \begin{bmatrix} 1 & 0.5 \\ 0.5 & 1 \end{bmatrix}.$$

The reason of choosing these particular examples is to elucidate the effect of $\mathbf{\Gamma}$ on the direction and speed of diffusion. If $\mathbf{\Gamma}$ is diagonal, the highest diffusion speed corresponds to the largest coefficient of $\mathbf{\Gamma}^{-1}$. In general the difusion direction is linked to the eigenvectors of $\mathbf{\Gamma}^{-1}$. However, if $\mathbf{\Gamma}$ is a full matrix, the diffusion direction is given by the eigenvector associated with the highest eigenvalue. If the two eigenvalues are equal, then heat is diffused along both eigenvectors directions with the same speed.

The initial density for the simulations is taken as the normalized Gaussian distribution, and the numerical domain is $[6 \times 6]$ with $\Delta x = \Delta y = 0.2$. The results for $\mathbf{\Gamma_1}$ are displayed in Figure 5, while the ones for $\mathbf{\Gamma_2}$ are in 6. We notice that in figure 5 the main diffusion direction is parallel to the horizontal axis, while 6 it is diagonal and aligned with the eigenvector corresponding to the highest eigenvalue. Evidently the approximate solution and the numerical one agree fully.

We also perform an order-of-convergence analysis for the simulation with $\mathbf{\Gamma_2}$. For it we keep the initial density and numerical domain as described before, while taking the number of cells in the x-direction and y-direction as 25, 50, 100 and 200. The simulations are run until the final time of $t_f = 0.1$, and then we compute the L^1 error with respect to the approximate solution via truncated Fourier series evaluated at $t = t_f$. The results for the first- and second-order schemes in 2D are displayed in table 3, and the order of convergence is indeed the correct one.

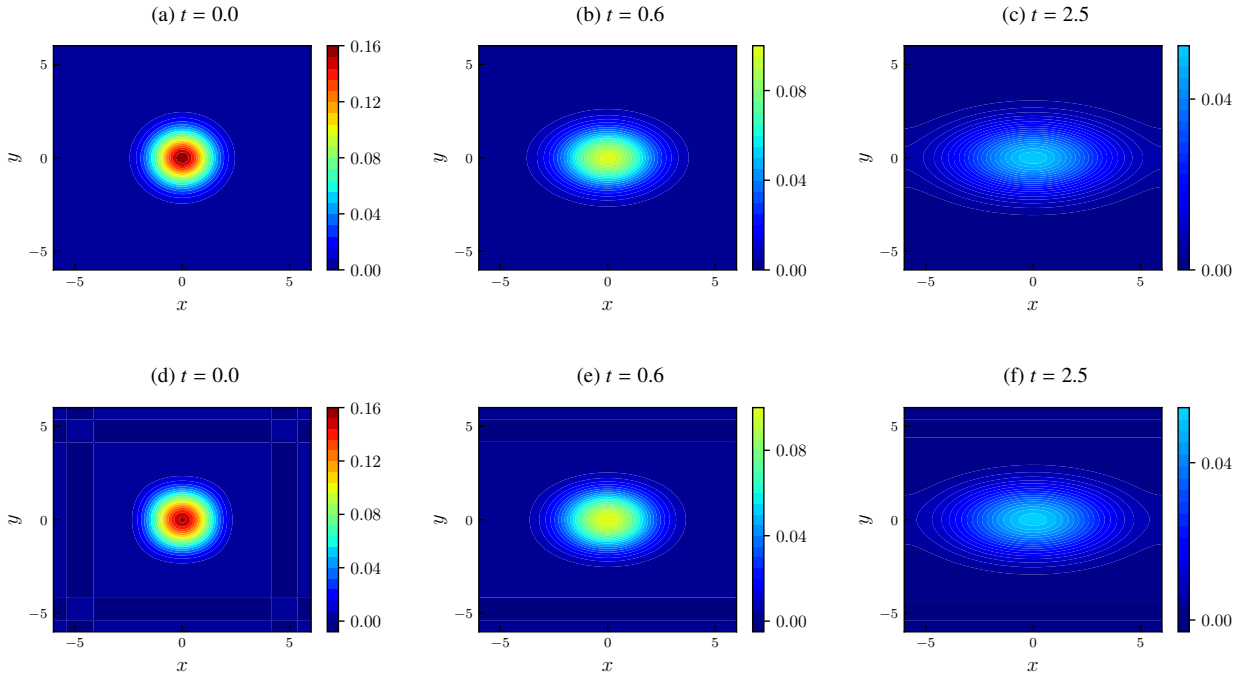

Fig. 5: Diffusion in $(1, 0)$ direction. (a)-(c) Numerical solution, (d)-(f) approximate (Fourier series) solution.

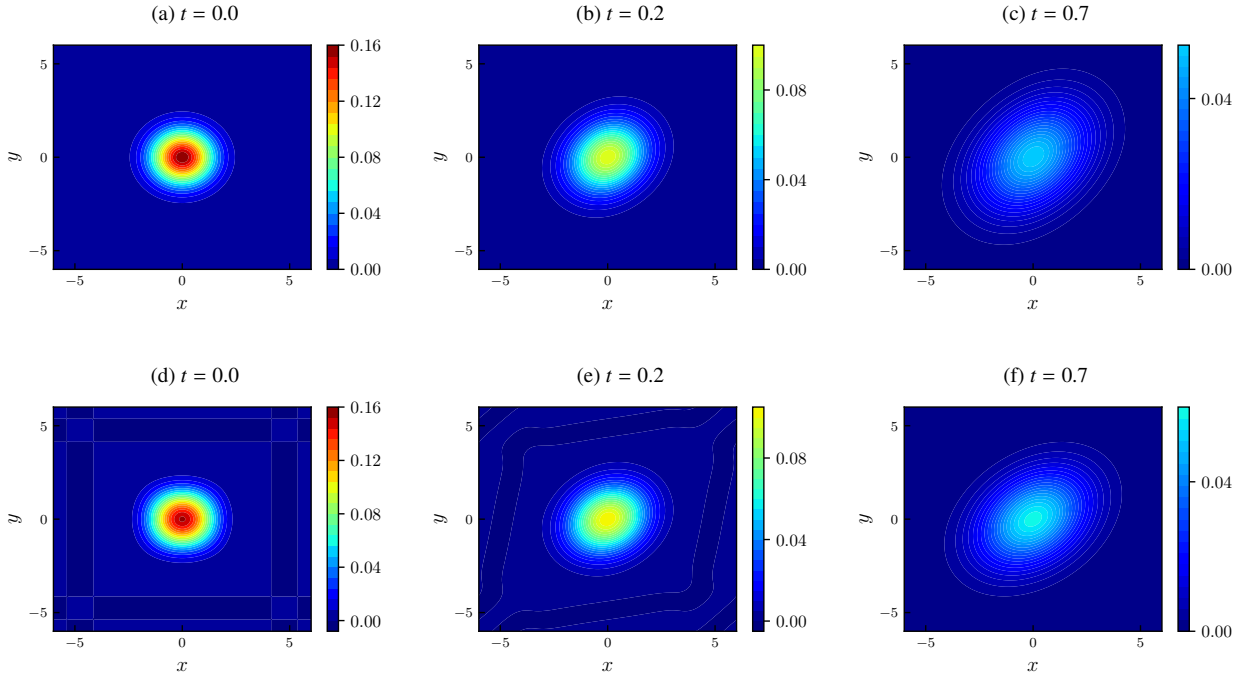

Fig. 6: Diffusion in (1,1) direction. (a)-(c) Numerical solution, (d)-(f) approximate (Fourier series) solution.

Table 3: Accuracy test for $\mathbf{\Gamma_2}$ with the first- and second-order schemes

Number of cells in x and y axis	First-order		Second-order	
	L^1 error	order	L^1 error	order
25	5.7587E-01	-	3.1048E-03	-
50	2.9196E-01	0.89	6.8529E-04	2.18
100	1.4919E-01	0.96	1.6196E-04	2.08
200	8.0392E-02	0.97	3.9546E-05	2.03

3.2.2. Space-dependent diffusion

Here we study the following non-homogenous diffusion problem with $\mathbf{\Gamma}^{-1}$ space dependent:

$$\frac{\partial \rho}{\partial t} = \nabla \cdot (\mathbf{\Gamma}^{-1} \nabla \rho). \tag{42}$$

This corresponds to (2) with the choices of $V = 0$, $H'(\rho) = \log(\rho)$ and $W = 0$. For simplicity we choose the following space-dependent $\mathbf{\Gamma}^{-1}$:

$$\mathbf{\Gamma}^{-1} = \Gamma^{-1}(x, y) \begin{pmatrix} 1 & 0 \\ 0 & 1 \end{pmatrix} = 1 + 100 \left| \cos\left(\frac{2\pi}{T} \sqrt{x^2 + y^2} \right) \right| \begin{pmatrix} 1 & 0 \\ 0 & 1 \end{pmatrix},$$

which sinusoidally varies in space.

The initial density for the simulations is taken as the normalized Gaussian distribution, and the numerical domain is $[6 \times 6]$ with $\Delta x = \Delta y = 0.2$. The resultsare displayed in Figure 7. Specifically, in Figures 7 (a)-(b)-(c) we plot the 2D numerical solution, while in Figures 7 (d)-(e)-(f) we depict specific slices of the numerical solution as well as of Γ^{-1} at $y = 0$. Figures 7 (e)-(f) shows that the slopes of the solution vary following the space-dependency of Γ^{-1}. Eventually ρ spreads out due to the diffusion.

Finally, in Figure 7 (g) we compare the discrete free energies of the heat equation in (42) with a diffusion coefficient of 50 and the non-homogenous diffusion problem with $\Gamma^{-1}(x, y) = 1 + 100 |\cos\left(\frac{2\pi}{T} \sqrt{x^2 + y^2}\right)|$. Evidently, the decrease of the free energy is faster for the nonhomogenous case.

3.2.3. Nonlinear diffusion equation in a radially-symmetric inhomogeneous medium 2D

Here we analyse the 2D extension of the 1D problem in equation (33). The equation was written in polar coordinates, but here we will make use of its Cartesian form for the 2D case. For this purpose one has to apply the following relationships:

- $\nabla \cdot F = \frac{1}{r} \frac{\partial}{\partial r}(r F_r) + \frac{1}{r} \frac{\partial F_\theta}{\partial \theta}$ with F a vectorial field,
- $\nabla f = \frac{\partial f}{\partial r} \hat{r} + \frac{1}{r} \frac{\partial f}{\partial \theta} \hat{\theta}$ with f a scalar field and $\hat{r} = (\cos(\theta), \sin(\theta))^T$, $\hat{\theta} = (-\sin(\theta), \cos(\theta))^T$.

If F and f are independent of θ, then: $\nabla \cdot F = \frac{1}{r} \frac{\partial}{\partial r}(r F_r)$ and $\nabla f = \frac{\partial f}{\partial r} \hat{r}$. In our case, we suppose that ρ satisfies this assumption and$\rho = \rho(r, t)$. By using the previous formulas, we get another form for (33):

$$\frac{\partial \rho}{\partial t} = \nabla \cdot (D \nabla \rho).$$

This equation is very similar to equation (42) in the previous example. Here we choose:

$$\mathbf{\Gamma}^{-1}(x, y) = D_0 r^a \rho^b \begin{pmatrix} 1 & 0 \\ 0 & 1 \end{pmatrix}, \tag{43}$$

and we select the rest of parameters as $\nu = 2$, $r = \sqrt{x^2 + y^2}$ and $w_\nu = 2\pi$. The initial condition for the simulations is,

$$\rho_0(r) = C_0(0) \left(1 - (r/r_0)^{2-a}\right)^{\frac{1}{b}},$$

where $a = 1$, $b = 3$, $r_0 = 0.14$ and $C_0(0)$ satisfies (35) with $M_\infty = 0.5$. The computational domain is $[-1, 1]^2$ with $\Delta x = \Delta y = 0.08$.

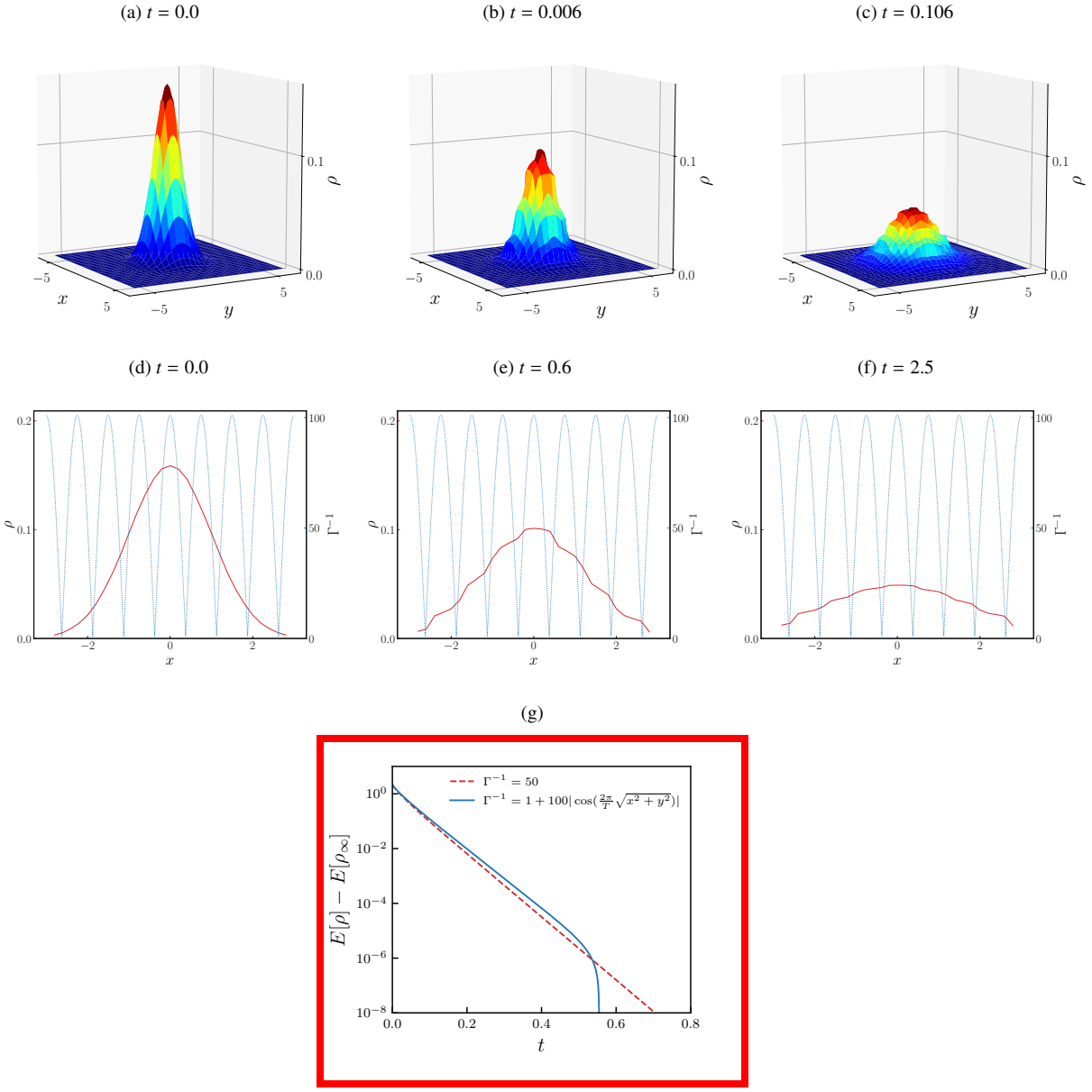

Fig. 7: (a)-(c) 3D plot of the numerical solution, (d)-(f) Slices of the numerical solution for $y = 0$, (g) Plot of $\Gamma^{-1}(x, 0)$. Parameter values: $\Gamma^{-1}(x, y) = 1 + 100|\cos\left(\frac{2\pi}{T}\sqrt{x^2 + y^2}\right)|$, $(T = 1.5)$, $\Delta x = \Delta y = 0.2$.

In Figures 8 (a)-(b)-(c) we plot the numerical solution obtained from our finite-volume scheme. We can observe how the compactly-supported density spreads out in time due to diffusion. In Figures 8 (d)-(e)-(f) we present slices at $y = 0$ of the numerical and the exact solutions (34) derived in [44].

Evidently the two slices are in good agreement and ρ spreads out radially over the domain.

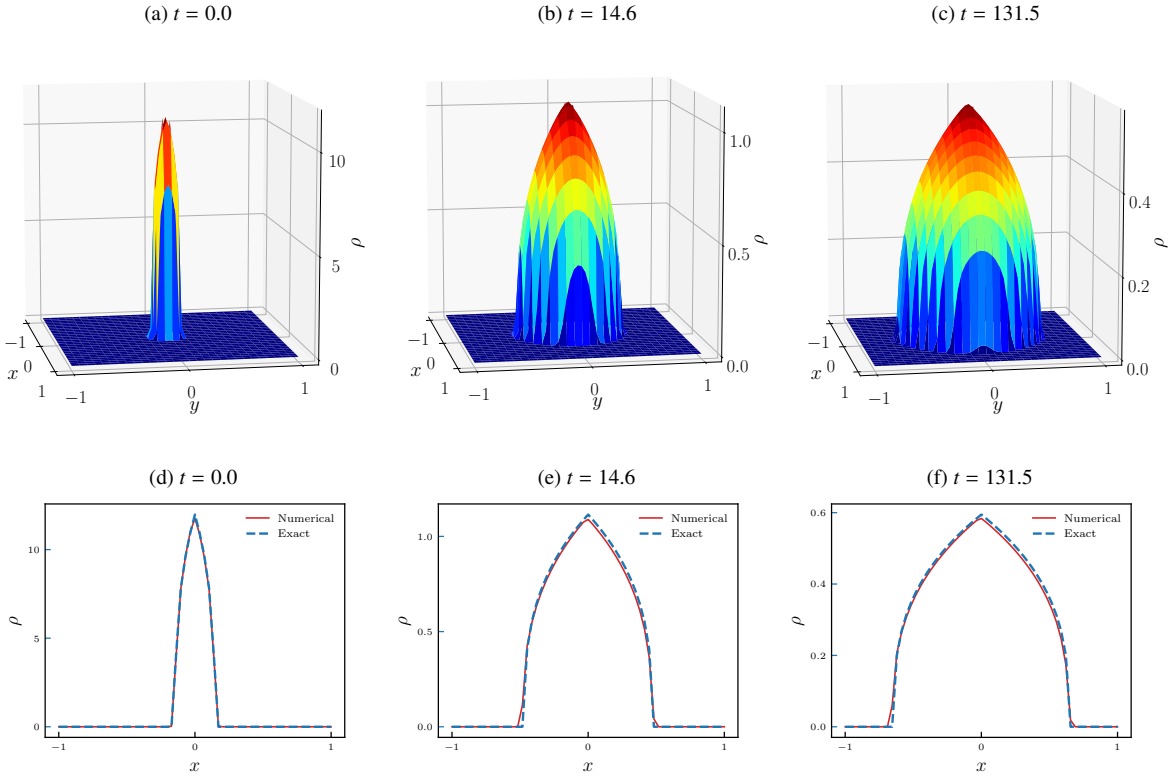

Fig. 8: (a): 3-D plot of the numerical solution, (b): Slices of numerical solution and exact solution for $y = 0$. Parameter values: $a = 1$, $b = 3$, $D_0 = 0.01$, $\Delta x = \Delta y = 0.08$, $r_0 = 0.14$, $M_\infty = 0.5$.

3.2.4. Nonlinear diffusion with nonlocal attraction in 2D

Here we consider the gradient flow in (2) with a non zero attraction kernel $W(x, y) = -\frac{1}{\pi}e^{-x^2-y^2}$:

$$\frac{\partial \rho}{\partial t} = \nabla \cdot \left(\mathbf{\Gamma^{-1}} \rho \nabla \cdot \left(\nu \rho^{m-1} + W(x, y) \star \rho \right) \right).$$

The aim of this example is to compare the dynamical evolution with two different $\mathbf{\Gamma^{-1}}$ matrices:

$$\mathbf{\Gamma_1} = \begin{bmatrix} 10 & 0 \\ 0 & 1 \end{bmatrix}, \quad \mathbf{\Gamma_2} = \begin{bmatrix} 1 & 0.5 \\ 0.5 & 1 \end{bmatrix}.$$

This choice is motivated by the fact that their eigenvectors have different directions which in turn results in varied directions of diffusion during the evolution. The space domain taken in the simulations is $[-3, 3]^2$ meshed with $\Delta x = \Delta y = 0.03$, and the initial condition satisfies $\frac{1}{4}\chi_{[-3,3]^2}(x, y)$.

Figures 9 (a)-(b)-(c)-(d) depict the evolution with $\mathbf{\Gamma_1}$. We observe a similar dynamics to the ones in the 1D example 3.1.4(a). In this case four identical bumps are formed, eventually merging into a single one. The non-local attraction (convolution) dominates the diffusion during the dynamical evolution, until the steady state is approached, while the dynamics is symmetric with respect to $(0, 0)$.

Figures 9 (e)-(f)-(g)-(h) show the results with $\mathbf{\Gamma_2}$. Although the steady state is identical with the case $\mathbf{\Gamma_1}$, we observe the merging of the two groups of peaks is accomplished at two different timescales. This is due to the different eigenvectors of $\mathbf{\Gamma_2}$ and $\mathbf{\Gamma_1}$. Indeed, in the discrete free-energy plot in Figure 9 (i) we notice that for $\mathbf{\Gamma_1}$ there is a a plateau before the merging followed by a drastic decrease of free energy. On the contrary, for $\mathbf{\Gamma_2}$ we notice from Figure 9 (i) that there are two distinct decreases of free energy due to the two mergings that take place during the evolution, as is evident from Figure 9 (c).

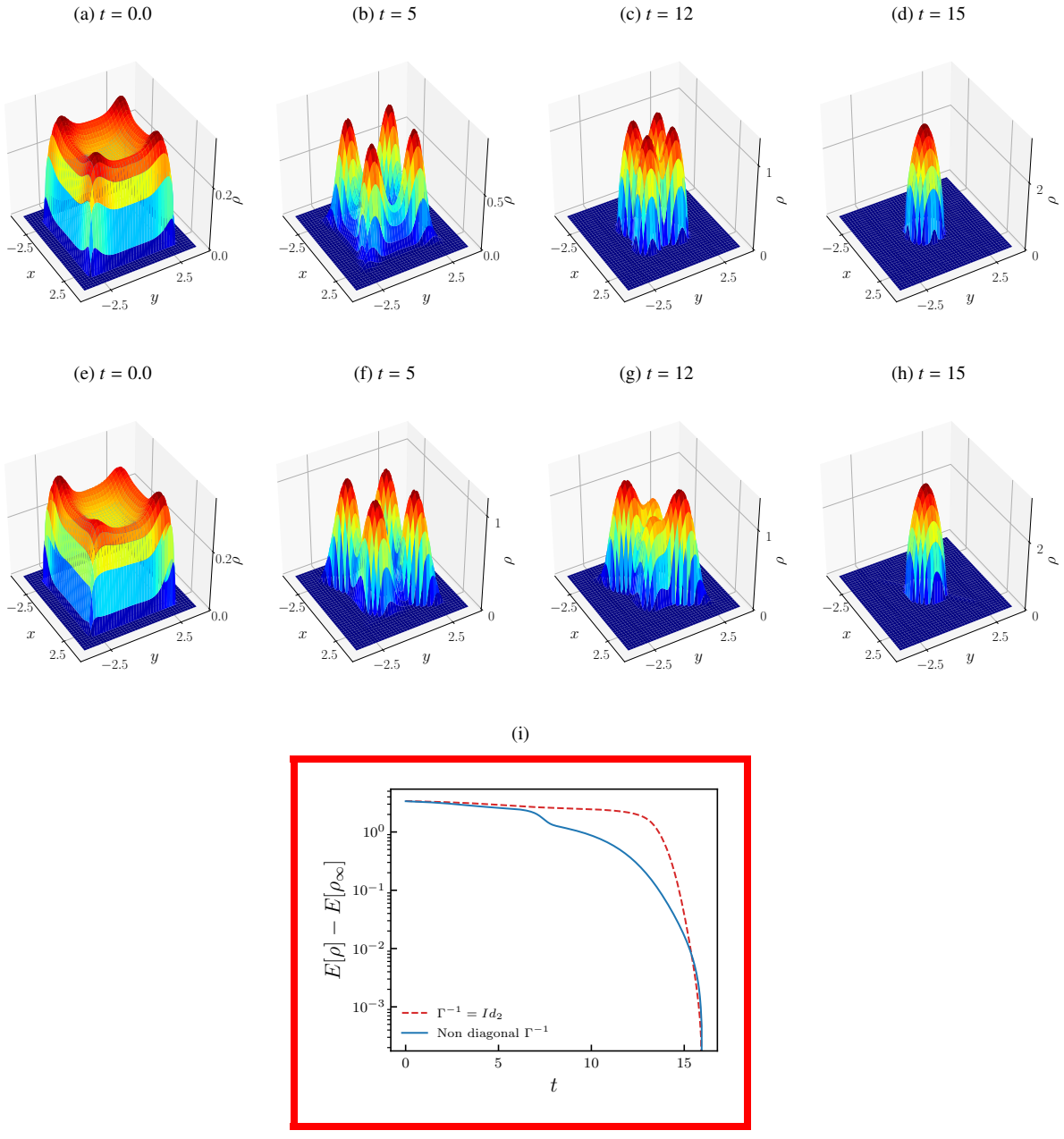

Fig. 9: (a)-(d): 3-D plot of the numerical solution with $\mathbf{\Gamma_1}$, (e)-(h): 3-D plot of the numerical solution with $\mathbf{\Gamma_2}$, (i): Decay of the discrete free energy. Parameter values: $m = 3$, $\Delta x = \Delta y = 0.05$, $\rho_0(x, y) = \frac{1}{4}\chi_{[-3,3]^2}(x, y)$.

4. Conclusions

We have developed an accurate, efficient and robust finite-volume scheme to solve gradient-flow equations with non-homogeneous properties. The equations are obtained in the framework of DDFT. Our numerical methodology extends the state-of-art in the finite-volume literature [34] by accounting for spatio-temporal dependence of the friction tensor $\mathbf{\Gamma}$.

We introduce 1D and 2D first- and second-order finite-volume schemes which satisfy the preservation of density positivity under a certain CFL condition as well as the discrete-energy decay. For both properties we provide proofs

for our finite-volume schemes. The schemes are constructed in an upwind fashion with a piecewise-constant reconstruction of the density for the first-order scheme and a linear non-negative reconstruction with minmod limiters for the second-order one.

The order of the scheme is tested for both homogeneous and non-homogeneous friction tensors demonstrating first- and second-order spatial convergence. Subsequently, we apply our approach to study several prototypical systems with thermal baths characterized by anisotropic, space-dependent and time-dependent properties, both in 1D and 2D. The dynamical evolution of density-profile and the decay of the discrete free energy allow us to scrutinise how the particular spatio-temporal dependency of $\mathbf{\Gamma}$ affects the dynamical evolution of the numerical solutions. We also performed several numerical experiments showing non-trivial dynamical evolutions arising from the particular choice $\mathbf{\Gamma}$ which in turn strongly influences the characteristic timescales of the system and decay rates of the discrete free energy. The schemes presented in this work could be employed in future works to study phenomena such as Turing patterns formation in non-homogeneous baths [28] and droplet impacts on heterogeneous substrates [45].

Acknowledgments

Antonio Russo acknowledges financial support from the Imperial College (IC) Department of Chemical Engineering PhD Scholarship scheme. Sergio P. Perez acknowledges financial support from the IC PhD President's Scholarhip scheme. Serafim Kalliadasis acknowledges financial support from ERC through Advanced Grant No. 247031 and EPSRC through Grants No. EP/L027186 and EP/L020564. The work was completed during the visit of Julien Mendes to IC as a UROP student.

References

[1] E. F. Keller, L. A. Segel, Initiation of slime mold aggregation viewed as an instability, Journal of theoretical biology 26 (1970) 399–415.
[2] P. M. Lushnikov, N. Chen, M. Alber, Macroscopic dynamics of biological cells interacting via chemotaxis and direct contact, Phys. Rev. E 78 (2008) 061904.
[3] C. M. Topaz, A. L. Bertozzi, M. A. Lewis, A nonlocal continuum model for biological aggregation, Bulletin of mathematical biology 68 (2006) 1601.
[4] J. Barré, P. Degond, E. Zatorska, Kinetic theory of particle interactions mediated by dynamical networks, Multiscale Model. Sim. 15 (2017) 1294–1323.
[5] R. J. McCann, A convexity principle for interacting gases, Advances in mathematics 128 (1997) 153–179.
[6] D. Benedetto, E. Caglioti, J. A. Carrillo, M. Pulvirenti, A non-maxwellian steady distribution for one-dimensional granular media, Journal of statistical physics 91 (1998) 979–990.
[7] D. D. Holm, V. Putkaradze, Formation of clumps and patches in self-aggregation of finite-size particles, Physica D: Nonlinear Phenomena 220 (2006) 183–196.
[8] P. Yatsyshin, A. O. Parry, C. Rascón, S. Kalliadasis, Wetting of a plane with a narrow solvophobic stripe, Mol. Phys. 116 (2018) 1990–1997.
[9] B. D. Goddard, A. Nold, S. Kalliadasis, Dynamical density functional theory with hydrodynamic interactions in confined geometries, J. Chem. Phys. 145 (2016) 214106.
[10] L. Landau, E. Lifshitz, Statistical physics, vol. 5, Course of theoretical physics (1980).
[11] K. Kawasaki, Stochastic model of slow dynamics in supercooled liquids and dense colloidal suspensions, Physica A 208 (1994) 35 – 64.
[12] D. S. Dean, Langevin equation for the density of a system of interacting langevin processes, J. Phys. A: Math. Gen. 29 (1996) L613.
[13] M. A. Duran-Olivencia, P. Yatsyshin, B. D. Goddard, S. Kalliadasis, General framework for fluctuating dynamic density functional theory, New J. Phys 19 (2017) 123022.
[14] A. Russo, M. A. Durán-Olivencia, S. Kalliadasis, R. Hartkamp, Macroscopic relations for microscopic properties at the interface between solid substrates and dense fluids, J. Chem. Phys. 150 (2019) 214705.
[15] R. Evans, The nature of the liquid-vapour interface and other topics in the statistical mechanics of non-uniform, classical fluids, Adv. Phys. 28 (1979) 143–200.
[16] U. M. B. Marconi, P. Tarazona, Dynamic density functional theory of fluids, J. Chem. Phys. 110 (1999) 8032–8044.
[17] A. J. Archer, M. Rauscher, Dynamical density functional theory for interacting brownian particles: stochastic or deterministic?, J. Phys. A 37 (2004) 9325–9333.
[18] B. D. Goddard, A. Nold, N. Savva, P. Yatsyshin, S. Kalliadasis, Unification of dynamic density functional theory for colloidal fluids to include inertia and hydrodynamic interactions: derivation and numerical experiments, J. Phys. Condens. Matter 25 (2012) 035101.
[19] B. D. Goddard, A. Nold, N. Savva, G. A. Pavliotis, S. Kalliadasis, General dynamical density functional theory for classical fluids, Phys. Rev. Lett. 109 (2012) 120603.
[20] J. F. Lutsko, A dynamical theory of nucleation for colloids and macromolecules, J. Chem. Phys. 136 (2012) 034509.
[21] J. F. Lutsko, M. A. Durán-Olivencia, Classical nucleation theory from a dynamical approach to nucleation, J. Chem. Phys. 138 (2013) 244908.
[22] A. Nold, D. N. Sibley, B. D. Goddard, S. Kalliadasis, Fluid structure in the immediate vicinity of an equilibrium three-phase contact line and assessment of disjoining pressure models using density functional theory, Phys. Fluids 26 (2014) 072001.
[23] P. Yatsyshin, N. Savva, S. Kalliadasis, Density functional study of condensation in capped capillaries, J. Phys. Condens. Matter 27 (2015) 275104.

[24] P. Yatsyshin, N. Savva, S. Kalliadasis, Wetting of prototypical one- and two-dimensional systems: Thermodynamics and density functional theory, J. Chem. Phys. 142 (2015) 034708.
[25] A. Nold, B. D. Goddard, P. Yatsyshin, N. Savva, S. Kalliadasis, Pseudospectral methods for density functional theory in bounded and unbounded domains, J. Comp. Phys. 334 (2017) 639 – 664.
[26] A. J. Archer, R. Evans, Dynamical density functional theory and its application to spinodal decomposition, J. Chem. Phys. 121 (2004) 4246–4254.
[27] J. Carillo, S. Kalliadasis, S. Perez, C.-W. Shu, Well-balanced finite-volume schemes for hydrodynamic equations with general free energy, arXiv preprint arXiv:1812.00980 (2020).
[28] A. Russo, M. A. Durán-Olivencia, P. Yatsyshin, S. Kalliadasis, Memory effects in dynamic density functional theory with fluctuation: Theory and simulations, J. Phys. A (2020).
[29] B. Goddard, G. Pavliotis, S. Kalliadasis, The overdamped limit of dynamic density functional theory: Rigorous results, Multiscale Model. Sim. 10 (2012) 633–663.
[30] C. Villani, Topics in optimal transportation, 58, American Mathematical Soc., 2003.
[31] J. A. Carrillo, R. J. McCann, C. Villani, et al., Kinetic equilibration rates for granular media and related equations: entropy dissipation and mass transportation estimates, Rev. Mat. Iberoam. 19 (2003) 971–1018.
[32] M. Burger, J. A. Carrillo, M.-T. Wolfram, A mixed finite element method for nonlinear diffusion equations, Kinet. Relat. Models 3 (2010) 59–83.
[33] M. Bessemoulin-Chatard, F. Filbet, A finite volume scheme for nonlinear degenerate parabolic equations, SIAM Journal on Scientific Computing 34 (2012) B559–B583.
[34] J. A. Carrillo, A. Chertock, Y. Huang, A finite-volume method for nonlinear nonlocal equations with a gradient flow structure, Commun. Comput. Phys. 17 (2015) 233–258.
[35] R. Bailo, J. A. Carrillo, J. Hu, Fully discrete positivity-preserving and energy-decaying schemes for aggregation-diffusion equations with a gradient flow structure, arXiv preprint arXiv:1811.11502 (2018).
[36] Z. Sun, J. A. Carrillo, C.-W. Shu, A discontinuous galerkin method for nonlinear parabolic equations and gradient flow problems with interaction potentials, J. Comp. Phys. 352 (2018) 76 – 104.
[37] L. N. De Almeida, F. Bubba, B. Perthame, C. Pouchol, Energy and implicit discretization of the fokker-planck and keller-segel type equations, arXiv preprint arXiv:1803.10629 (2018).
[38] A. Russo, S. P. Perez, M. A. Durán-Olivencia, P. Yatsyshin, J. A. Carrillo, S. Kalliadasis, A finite-volume method for fluctuating dynamical density functional theory, J. Comp. Phys. (2020) 109796.
[39] J. A. Carrillo, K. Craig, F. S. Patacchini, A blob method for diffusion, Calculus of Variations and Partial Differential Equations 58 (2019) 53.
[40] K. Craig, A. Bertozzi, A blob method for the aggregation equation, Mathematics of computation 85 (2016) 1681–1717.
[41] J. Carillo, M. J. Castro, S. Kalliadasis, S. Perez, High-order well-balanced finite volume schemes for hydrodynamic equations with nonlocal free energy, arXiv preprint arXiv:2004.05341 (2020).
[42] L. Pareschi, M. Zanella, Structure preserving schemes for nonlinear fokker?planck equations and applications, J. Sci. Comput. 74 (2018) 1575–1600.
[43] S. Gottlieb, C.-W. Shu, Total variation diminishing Runge-Kutta schemes, Math. Comput. Am. Math. Soc. 67 (1998) 73–85.
[44] M. Hayek, An exact solution for a nonlinear diffusion equation in a radially symmetric inhomogeneous medium, Comput. Math. Appl. 68 (2014) 1751–1757.
[45] A. Russo, M. Icardi, M. Elsharkawy, D. Ceglia, P. Asinari, C. M. Megaridis, Numerical simulation of droplet impact on wettability-patterned surfaces, Phys. Rev. Fluids 5 (2020) 074002.